Numerical analysis to study the tensile behaviour of a spring-steel-wire-reinforced aluminium alloy metal matrix composite

Matthias Merzkirch, Marius Meissner, Volker Schulze, Kay A. Weidenmann

Angaben zur Veröffentlichung / Publication details:

Merzkirch, Matthias, Marius Meissner, Volker Schulze, and Kay A. Weidenmann. 2015. "Numerical analysis to study the tensile behaviour of a spring-steel-wire-reinforced aluminium alloy metal matrix composite." *Journal of Composite Materials* 49 (21): 2659–71. https://doi.org/10.1177/0021998314553044.

Numerical analysis to study the tensile behaviour of a spring-steel-wire-reinforced aluminium alloy metal matrix composite

Matthias Merzkirch, Marius Meissner, Volker Schulze and Kay André Weidenmann

Abstract

The reinforcement of composite extruded light metal profiles offers a high potential in terms of weight reduction and the improvement of mechanical properties, both of which are essential for components in lightweight space frame constructions. In a previous study, the mechanical properties under tensile loading of spring-steel (301SS)-wire-reinforced aluminium extrusions based on EN AW-6082 were investigated in terms of a varying reinforcing ratio. The aim of the current study is to minimize the effort needed to gather mechanical data by calculation of the deformation and damage behaviour under tensile loading of 11.1 vol.% spring-steel-reinforced EN AW-6082. The simulation of the push-out test provided specific parameters concerning the interfacial properties – like the radial strength – needed for modelling the tensile test. It could be shown that the simulation of the tensile test is in good agreement with the experimental results, concerning quantitative values (stress–strain curve) and qualitative behaviour (necking and debonding).

Keywords

Finite element analysis, EN AW-6082, interfacial strength, push-out test, composite extrusion

Introduction

Production process: Composite extrusion

The composite extrusion process, which is outlined in Kleiner et al.,[1] allows a direct embedding of metallic wires and hybrid wires based on ceramic fibres[2–5] within lightweight metal matrices such as aluminium and magnesium alloys with the help of modified porthole dies. A multitude of different continuous wire-reinforced material combinations and profile geometries have been produced with a maximum reinforcing ratio of 13.5 vol.%.[6]

Interfacial characterization: Push-out test

For a first estimation of the quality of extruded profiles, statements about the quality of the embedded reinforcing elements (REs) are necessary. A simple method (regarding specimen preparation and experimental setup) to determine the interfacial strength (debonding shear strength) of unidirectionally reinforced composites is the push-out test proposed by Marshall[7] and Marshall and Oliver.[8] The functional principle is depicted in Figure 1.

The RE (diameter d) within the flat specimen (thickness h) is loaded axially by an indenter. A groove (width b) within the support area allows the RE to be pushed out of the surrounding matrix (M) material. During this displacement controlled test, the load is measured continuously. After reaching the maximum load F_{max}, the interface collapses, and the RE is subsequently pushed out, generating friction between the RE and the matrix material.[10–12] The maximal debonding shear strength is calculated using the maximum load

Institute for Applied Materials (IAM–WK), Karlsruhe Institute of Technology (KIT), Karlsruhe, Germany

Corresponding author:
Matthias Merzkirch, Institute for Applied Materials (IAM–WK), Karlsruhe Institute of Technology (KIT), Engelbert-Arnold-Strasse 4, 76128 Karlsruhe, Germany.
Email: Matthias.Merzkirch@kit.edu

and the lateral area of the RE[7] (Figure 1), according to equation (1):

$$\sigma_{deb} = \frac{F_{max}}{\pi \cdot d \cdot h} \quad (1)$$

Ideally, the interface only experiences shear loads. In practice, due to the lateral expansion by the compression load, a certain normal stress occurs.[13] A further disadvantage is that the groove of the support area should be larger than the diameter of the RE. As a consequence, in addition to the axial loading of the RE, a bending of the specimen occurs, which is influenced by the diameter of the RE, the specimen thickness and the groove width.[13] Nevertheless, this experimental method is predestined for a quick and easy quantification of the interfacial bonding. It was used for different material systems.[3,9] Unfortunately it does not deliver any insight into the normal debonding strength. In Theler et al.,[14] the normal adhesion strength of composite extruded aluminium/steel profiles was determined to be about 200 MPa, which corresponds to about 90% of the ultimate tensile strength of the aluminium alloy EN AW-6060. The measured shear strength was about 140 MPa.[14]

Tensile behaviour of monofilament-reinforced composites

A detailed investigation of the tensile deformation and damage behaviour in longitudinal direction of the monofilament spring-steel (301SS)-wire-reinforced aluminium alloy EN AW-6082 (Mg and Si alloyed) with varying reinforcing ratio is presented in Merzkirch et al.[15] The investigations have shown that the ductility of the RE leads to higher ductility of the composite, as is predicted by the Kelly model of Kelly and Davies[16] and Courtney.[17] A representative nominal stress–total strain curve for an 11.1 vol.% spring-steel-wire-reinforced EN AW-6082 composite is shown in Figure 2. For comparison, Figure 2 also includes the unreinforced monolithic matrix material.

According to the Kelly model,[16,17] within region I pure elastic behaviour occurs where the rule of mixture for the Young's modulus E_I can be used. The beginning of region II is defined by the onset of plasticity of the matrix material at its yield strength $\sigma_{y,M}$. The superposition of the elastic behaviour of the RE and the elastic–plastic behaviour of the matrix material within region II can be approximated by equation (2):

$$E_{II} = E_{RE} \cdot V_{RE} + \left(\frac{d\sigma_M}{d\varepsilon_M}\right) \cdot V_M \quad (2)$$

The differential coefficient $\left(\frac{d\sigma_M}{d\varepsilon_M}\right)$ describes the slope of the stress–strain curve after the onset of plasticity and marks the linear approach of the hardening of the unreinforced matrix material. Since the slope during hardening is gradual in comparison to the Young's modulus of the RE, equation (2) can be simplified by neglecting the second term. Region III is determined by the plastic deformation of the RE and does not occur where brittle REs are used.[16,17] In Merzkirch et al.,[15] metallographic examination showed multiple necking of the RE. Additionally, the necking of the matrix material in turn leads to a debonding of the interface between the RE and the matrix material.[15] The ultimate

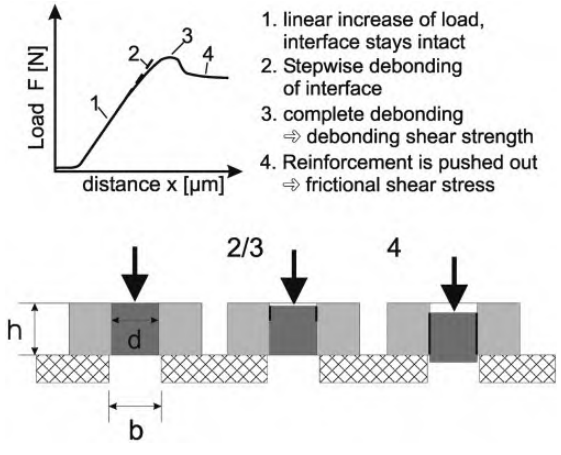

Figure 1. Functional principle and schematic load–displacement curve of a push-out test according to Weidenmann et al.[9]

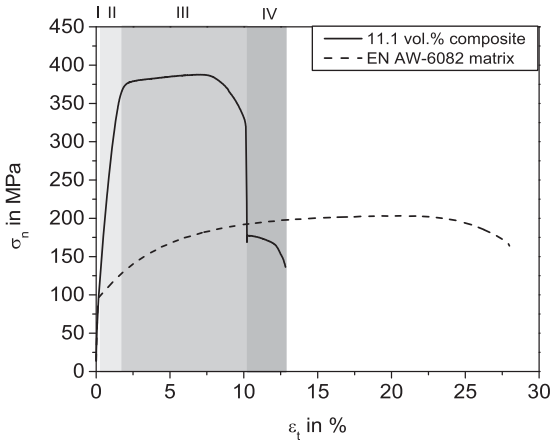

Figure 2. Representative nominal stress (σ_n)-total engineering strain (ε_t) curve of an 11.1 vol.% reinforced specimen (tested in longitudinal direction) with indications of the different deformation and damage regions I–IV, and for comparison the unreinforced matrix material EN AW-6082.[15]

tensile strength of the composite can be calculated as follows:

$$\sigma_{\mathrm{UTS,C}} = \sigma_{\mathrm{UTS,RE}} \cdot \mathrm{V_{RE}} + \sigma_{\mathrm{M}}\left(\varepsilon_{\mathrm{RE}}^{\mathrm{F}}\right) \cdot \mathrm{V_M} \qquad (3)$$

$\sigma_{\mathrm{M}}\left(\varepsilon_{\mathrm{RE}}^{\mathrm{F}}\right)$ stands for the stress occurring within the matrix at fracture of the RE.[16,17] The fracture of the RE marks the transition to region IV which represents the elastic–plastic behaviour of the remaining matrix until its final fracture at a total strain of about $\varepsilon_{\mathrm{t}} \approx 13\%$.[15]

Since the main aim of simulations is to reduce elaborate experimental investigations, the present study deals with the calculation of the tensile behaviour of 11.1 vol.% spring-steel-wire-reinforced aluminium alloy EN AW-6082 and the comparison with experimental tensile tests, shown in Merzkirch et al.[15] The first step of the modelling includes the implementation of the mechanical tensile data of the single components, RE and matrix. For the modelling of the contact between the RE and the surrounding matrix material, more quantitative information about the interfacial behaviour is needed, since the experimental data about the debonding behaviour are relatively poor. Therefore, the push-out test was also calculated including the iterative implementation of interfacial parameters, aiming for a proper adaption of the interfacial properties to the model of the tensile test.

Modelling

The modelling of the push-out test and tensile test was performed by ABAQUS Standard 6.10. Two-dimensional axisymmetric quadrilateral elements[18] with reduced integration (CAX4R) were used.

Push-out test

Similar to the experimental setup shown in Figure 1, the push-out test was modelled on an axisymmetric half section, according to Marshall and Oliver[8] and Chandra and Ananth,[18] due to the existing symmetries (see Figure 3). The indenter was modelled as a sphere with infinite stiffness (rigid body).

Due to the axisymmetric character of the model, the groove was modelled as circular gap, whereas it is rectangular within the experiment.[9] The support area with a length of 3 mm was modelled as fix gripping with neither translational nor rotational degrees of freedom. The displacement of the indenter is allowed by appropriate boundary conditions in the y-direction. The meshing, see Figure 3, was modelled by a refinement towards the interface.

Tensile test

The geometry of the tensile specimen with a reinforcing ratio of 11.1 vol.% is shown in Figure 4. The RE with a

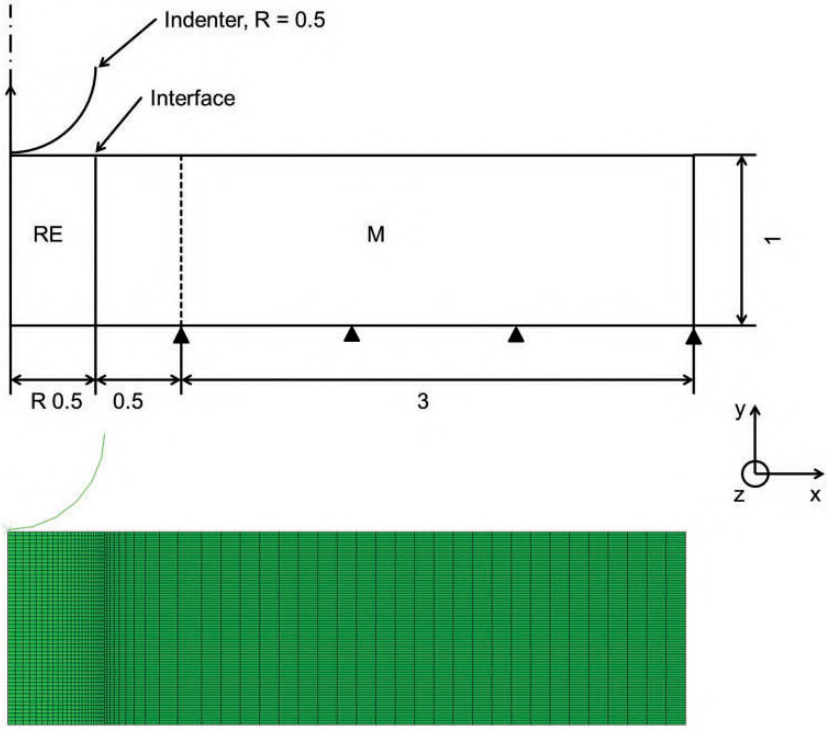

Figure 3. Model (above) and meshing (below) of the push-out specimen, dimensions in mm.

constant diameter of 1 mm is placed in the centre of the cylindrical specimens (dotted line).

The tensile specimen was modelled as an axisymmetric quarter section with respect to the symmetric character of the specimen (see Figure 5). As a boundary condition for the axis of symmetry, the displacement in the y-direction as well as the rotation around the x- and z-axis was limited ($U_y = 0$, $UR_x = UR_z = 0$).[19]

The displacement-controlled loading was realized via boundary conditions at the clamping area of the specimen's outer surface – the length of which is exactly the same as in the experiment – in a positive y-direction.

The small element size of the RE is the result of the demand that the size of the element of a 'master' contact area should be bigger that of the 'slave' contact area of a cohesive joint.[19] The level of mesh refinement in the gauge section has been shown to be sufficient to capture the desired effects. Since the focus of the investigations is on the gauge length, the element size of the clamping area is chosen to be larger in order to save computing time. The strain was determined along the modelled measuring length.

Modelling of the interface

Generally the modelling of the interface can be carried out based on a cohesive layer with known thickness or by knowledge of the mechanical data, e.g. the shear modulus.[18] Due to missing experimental data, a simpler and established method was chosen: modelling a spring layer as an interface layer with a neglectable thickness. As described in the literature[18,20–23] in detail, the RE and matrix are coupled by stiff springs as surface knots.

Since no displacement of the contact areas of the single components is possible, the stiffness of the spring should be a multiple larger than the Young's modulus of the components. In order to prevent convergence problems, the values are limited. As an example, in Chandra and Ananth[18] a stiffness 100 times higher than that of the RE was chosen. The linear elastic displacement model includes the stress tensor **t**, including the stress in normal (radial) direction and the components for shear and torsion which can be calculated from the displacement δ_{Sim} and the stiffness matrix K:[19]

$$t = \begin{Bmatrix} t_n \\ t_s \\ t_t \end{Bmatrix} = \begin{bmatrix} K_{nn} & K_{ns} & K_{nt} \\ K_{ns} & K_{ss} & K_{sn} \\ K_{nt} & K_{st} & K_{tt} \end{bmatrix} \cdot \begin{Bmatrix} \delta_n \\ \delta_s \\ \delta_t \end{Bmatrix} = K \cdot \delta_{Sim} \tag{4}$$

K_{nn}, K_{ss} and K_{tt} represent the stiffness in the normal and the two shear directions which were assumed to be $K_{nn} = K_{ss} = K_{tt} = 5 \times 10^5$ GPa in order to ensure a stable calculation.

Generally the interface bond in radial normal direction is another unknown variable. As a rough estimate, in Mukherjee et al.[21] the value for the interface normal bond was set equal to the interface debonding shear strength, in which a significant overestimation was observed. Until damage initiation there is a linear correlation between stress and strain. After damage initiation, damage evolution occurs in terms of the degradation rate and the type of interface stiffness. The current investigations include the quadratic stress

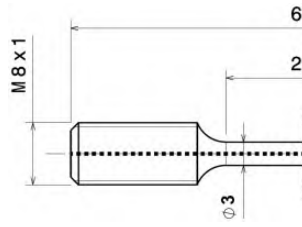

Figure 4. Specimen geometry with a reinforcing ratio of 11.1 vol.% with dimensions in mm.

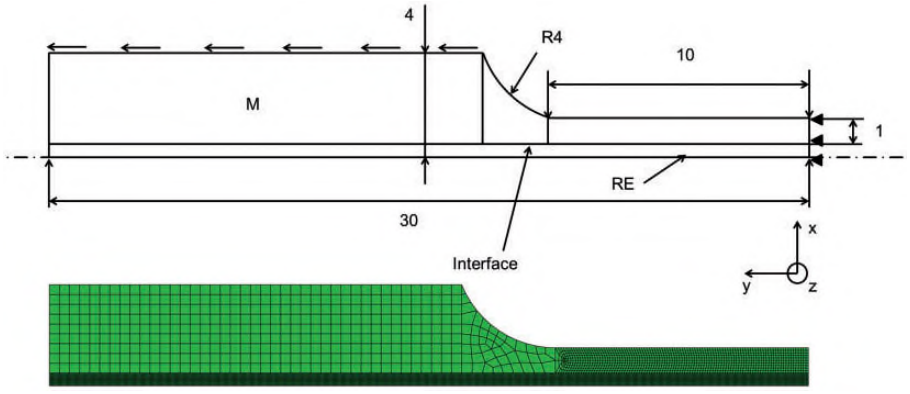

Figure 5. Model (above) and meshing (below) of the tensile specimen.

criterion proposed by Mukherjee et al.[21] and Wisnom[24] where a combination of the normal and shear stress is considered for the calculation of the damage initiation of the interface:

$$\left\{\frac{t_n}{t_n^0}\right\}^2 + \left\{\frac{t_s}{t_s^0}\right\}^2 + \left\{\frac{t_t}{t_t^0}\right\}^2 = 1 \quad (5)$$

For damage evolution, the scalar damage variable D_{Sim} with linear degression was introduced. Damage initiation is represented by the value 0. During damage evolution this value is steadily increased from 0 to 1

$$t_n = \begin{cases} (1 - D_{Sim}) \cdot \bar{t}_n, \bar{t}_n \geq 0 \\ \bar{t}_n, \qquad \text{else} \end{cases} \quad (6)$$

$$t_s = (1 - D_{Sim}) \cdot \bar{t}_s \quad (7)$$

$$t_t = (1 - D_{Sim}) \cdot \bar{t}_t \quad (8)$$

The default of damage evolution can be declared by the maximum displacement δ_{Sim} of total failure of the contact point or by the maximum fracture energy which is used at the failure of the contact point. The fracture energy at failure of the interface was iteratively assumed to be 2 kJ/m^2.

Material parameters

Detailed information about the experimental procedure and the investigation of the quasi-static behaviour under tensile loading of the matrix and reinforcing component is discussed in Merzkirch et al.[15] The experimentally determined material data (stress–strain curve with elastic and elastic–plastic parts) of the single components, the aluminium matrix material EN AW-6082 and the reinforcing spring-steel (301SS)-wire with a diameter of 1 mm, shown in Figure 6, were implemented into ABAQUS. The RE and the matrix are regarded as isotropic and homogeneous and the ABAQUS classical metal plasticity model with isotropic hardening was employed.

An overview of the quasi-static properties of the matrix material and the RE is presented in Tables 1 and 2, respectively,[15] where E is the Young's modulus of the matrix (index M) and the RE (index RE). $R_{p0.2}$ is the offset yield strength and σ_{UTS} is the ultimate tensile strength. ε^{uni} is the uniform elongation and ε^F

Table 1. Quasi-static properties of the matrix material EN AW-6082.

E_M		$R_{p0.2}$		$\sigma_{UTS,M}$		ε_M^{uni}	ε_{RE}^F
in GPa	in %	in MPa	in %	in MPa	in %	in %	in %
68	± 2.9	99	± 1.3	202	± 1	20.7 ± Δ 1.6	28 ± Δ 0.2

Table 2. Quasi-static properties of the reinforcing element 301SS.

E_{RE}		$R_{p0.2}$		$\sigma_{UTS,RE}$		ε_{RE}^{uni}	ε_{RE}^F
in GPa	in %	in MPa	in %	in MPa	in %	in %	in %
197	± 1.4	1963	± 0.5	2095	± 0.2	1.7 ± Δ 0.02	1.8 ± Δ 0.07

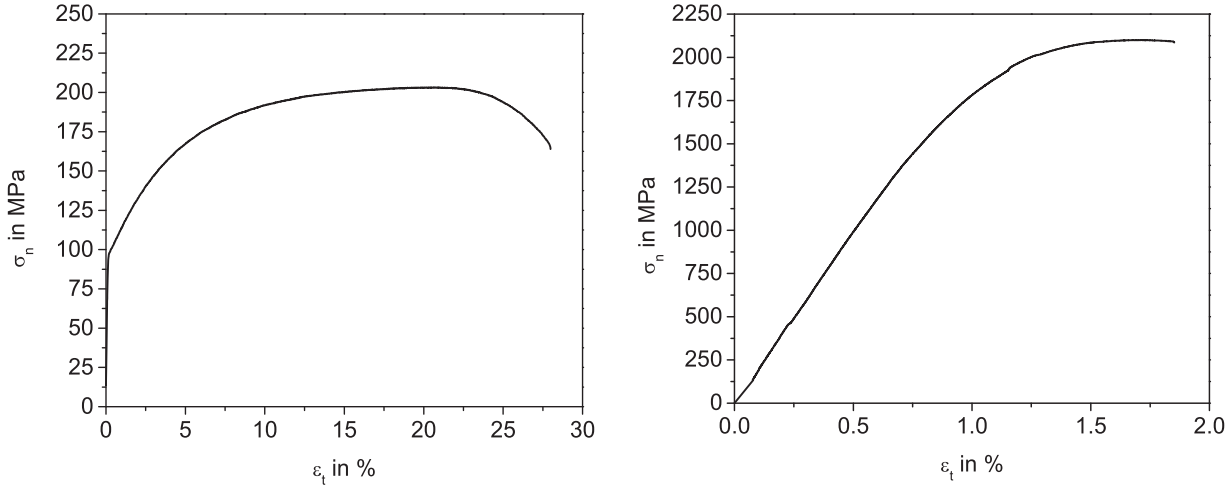

Figure 6. Representative experimental nominal stress–total engineering strain curves of the matrix material (left) and the RE (right).[15]

the elongation until fracture of the component occurs. It should be noted that the wire shows plastic deformation.

The interfacial strength was determined via the push-out test on a flat specimen with a thickness of 1 mm to $\sigma_{deb} = 73$ MPa. The RE – diameter d within the flat specimen (thickness h) was loaded axially by an indenter. The groove within the support area had a width of 2 mm. Further details can be found in Weidenmann et al.[9]

Results and discussion

Push-out test

The simulation of the push-out test was primarily carried out for verification of the interfacial properties, since these are needed for the simulation of the tensile test. Since no proven statement – experimental data – about the value of the normal strength between the RE and matrix material can be issued, the normal strength was assumed to be equal to the interfacial shear strength ($\sigma_{deb} = 73$ MPa), according to Mukherjee et al.,[21] as an initial value. Since no debonding of the interface was observed during simulation using this value, much smaller values were then used – varying between 2, 3 and 4 MPa – and implemented for an iterative evolution of the experimentally determined values.

The influence of the radial normal strength σ_{rad} on the load–displacement curve is shown in Figure 7. The fracture energy correlates with the area beneath the load–displacement curve.

Furthermore, it can be seen that the interfacial normal strength only affects the maximum load, whereas the displacement at the maximum load and the total energy is almost constant (~ 20 µm). A doubling of the interfacial normal strength leads to an increase in the maximum load of 13 N. The choice of the interfacial normal strength was made by iteration of the simulation of the tensile tests. For the following investigations a radial normal strength of $\sigma_{rad} = 2$ MPa was assumed.

Figure 8 shows the comparison of the experimental data with the calculated load–displacement curve. At the beginning of the test a high stiffness can be seen. A possible explanation can be found in the modelling of the groove as a circular gap. This may lead to a higher initial stiffness than the rectangular groove in the experiment. Further comparison of the curves after reaching the maximum load is omitted in the following discussion, since friction effects beyond the load drop were neglected in the calculations.

Since a relatively good agreement was shown between the calculation and the experiment for damage initiation before reaching the maximum load, the following section deals with the analysis of the different stress components in the interfacial area using contour plots.

Figure 9 shows the shear strength along the interface for different displacements. At the beginning of the test, Figure 9(a), relatively small shear stresses in loading direction within the area of the load initiation at the top and bottom of the specimen can be seen. The highest shear stress can be observed in the centre section of the specimen. At higher penetration depths, Figure 9(b), an increase in the shear strength can be seen at the top and bottom of the specimen. At a penetration depth of 30 µm a relatively homogeneous shear loaded area can be observed. At the top of the specimen close to the interface and at the bottom of the specimen high deformation of the matrix material can be found (see arrows Figure 9(c)).

Figure 10 depicts the radial stress within the RE as well as within the matrix material with increasing

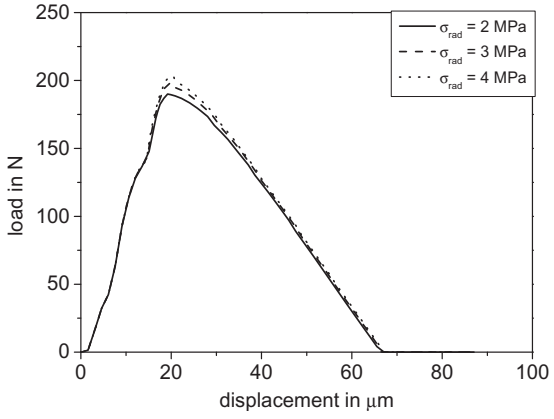

Figure 7. Influence of the radial normal strength on the load–displacement curve.

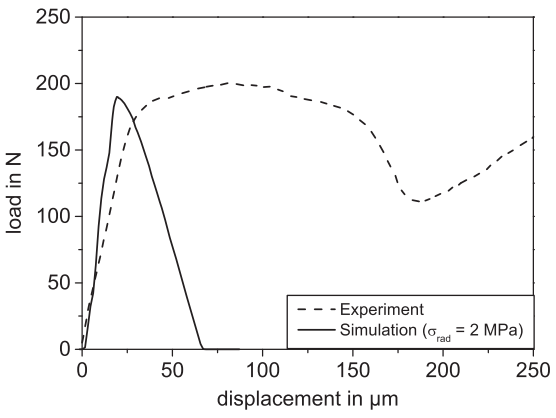

Figure 8. Comparison between calculated ($\sigma_{rad} = 2$ MPa) and experimentally determined load–displacement curve.

displacement. In particular, at the area of the load initiation, high radial compressive stresses can be seen which can be attributed to the radial deformation of the RE resulting from the axial loading as well as the load flow between the RE and matrix material.

Furthermore, the radial tensile stresses close to the interface can be observed at the bottom of the specimen. The stress resulting from the contact with the support area can also be seen in Figure 10(b) and (c).

In order to investigate the influence of the interfacial damage from the different displacements, Figure 11 shows the qualitative damage state of the interface via cohesive surface damage (CSDMG),[19] analogous to D_{sim}, see equations (6) to (8). Red areas represent complete delamination (CSDMG = 1), whereas blue areas represent a completely intact interface (CSDMG = 0).

It can be observed that damage initiation of the interface occurs at the bottom of the specimen.

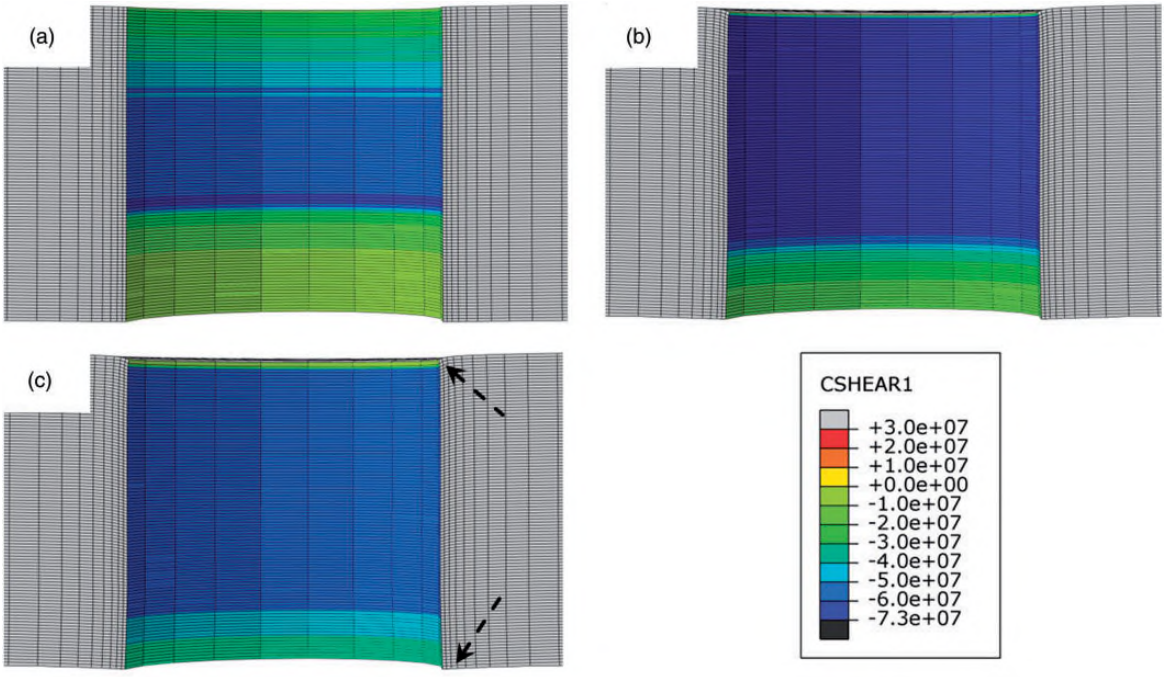

Figure 9. Evolution of the shear stress (in Pa) in axial direction at displacements of (a) 10 μm, (b) 20 μm, (c) 30 μm (scale factor = 10).

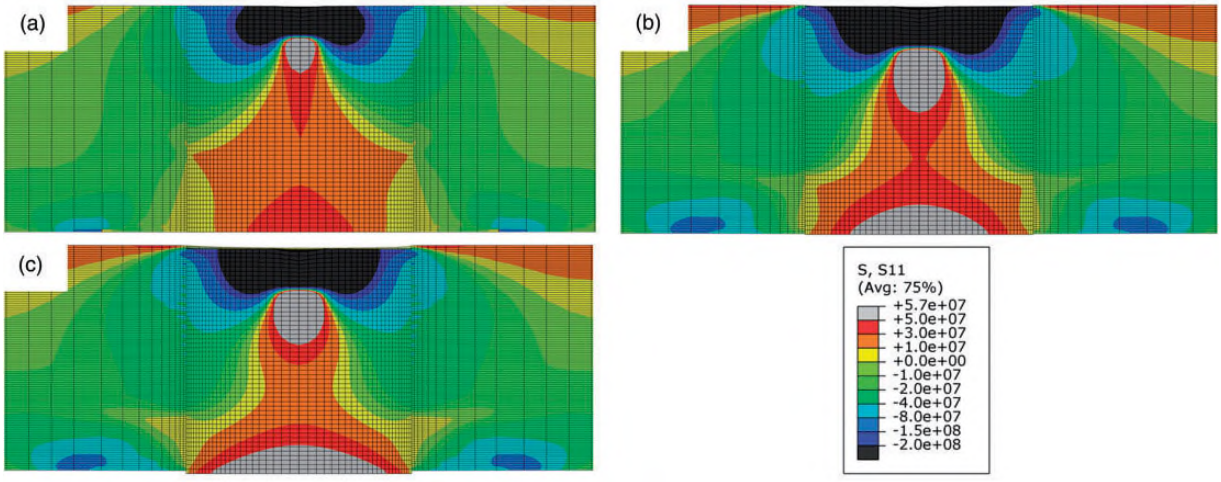

Figure 10. Calculated radial stress (in Pa) at displacements of (a) 10 μm, (b) 20 μm, (c) 30 μm (scale factor = 1).

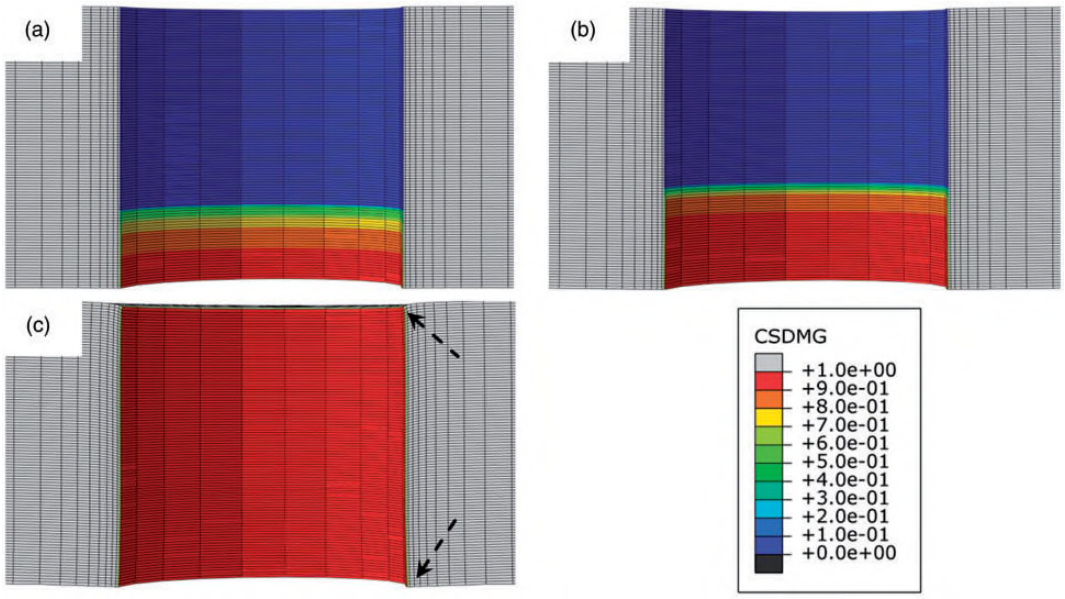

Figure 11. Qualitative evolution of interface damage at displacements of (a) 10 μm, (b) 20 μm, (c) 30 μm (scale factor = 10).

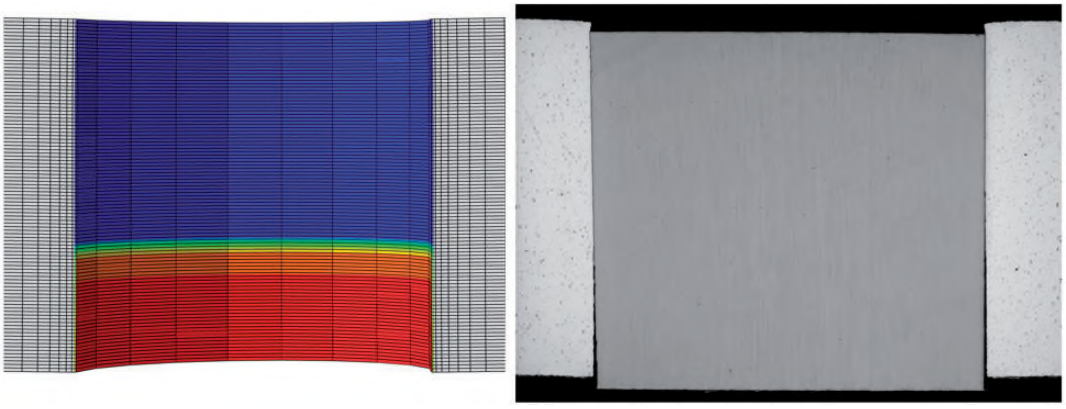

Figure 12. Comparison between calculated (scale factor = 1) (left) and experimentally determined (right) interface damage.

The amount of delamination rises with increasing penetration depth bottom-up. At a penetration depth of 20 μm, Figure 11(b), the interfacial damage occurred at about one-third of the specimen thickness, where already a complete delamination occurs at a penetration depth of 30 μm. Furthermore, the deformation at the top as well as at the bottom can be seen (arrows in Figure 11(c)), compare Figure 9.

Figure 12 compares the calculated (left) and the experimentally determined (right) damage. A similar plastic deformation of the matrix material at the top edge of the specimen can be observed for the dragged matrix material. Furthermore, a comparable delamination at the bottom specimen area is seen in both investigations. In addition, plastic deformation of the matrix material at the top as well as at the bottom of the specimen can be seen. It can be concluded that the high radial tensile stresses at the bottom of the specimen, resulting from bending, lead to a delamination of the interface.

It can be observed that the assumed interfacial normal strength of 2 MPa might be too small. The (macromechanically) measured adhesion strength of steel/aluminium joints close to the ultimate tensile strength of the matrix material,[14] which was initially chosen, is much too high. This has already been proved by assuming the interfacial normal strength to be equal to the interfacial shear strength.[24]

Tensile test

The stress–strain curve of the composite calculated from the mechanical behaviour of the single

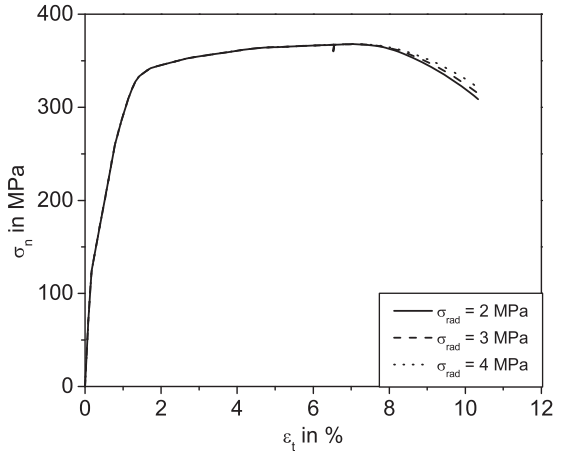

Figure 13. Calculated nominal stress–total engineering strain curve at different radial normal strengths of the interface.

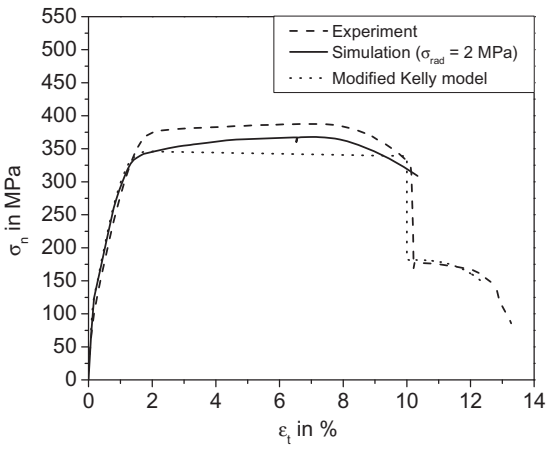

Figure 14. Comparison between the nominal stress–total engineering strain curves obtained via simulation ($\sigma_{rad} = 2$ MPa), calculation using the modified Kelly model[15] and experiment.[15]

components is depicted in Figure 13. The influence of different implemented maximal radial normal strengths σ_{rad} of the interface – varying between 2, 3 and 4 MPa – can be observed.

For all curves a steep increase up to 125 MPa, followed by a gradual flattening of the curve can be observed.

The stress plateau region starts at a total strain of about $\varepsilon_t \approx 2\%$. For a radial normal strength of $\sigma_{rad} = 2$ MPa small stress decreases are visible at a total strain of about $\varepsilon_t = 6.5\%$. The cause of this was not clarified. From a total strain of $\varepsilon_t \approx 7.6\%$ a stress reduction can be seen showing the influence of the radial bond. An increasing flattening of the stress reduction – a less pronounced stress reduction – can be observed with increasing radial bond. The simulation was interrupted at a strain of 10.3% since only the deformation and debonding behaviour up to the end of region III is of interest. Furthermore, elaborate experimental data about the detailed fracture behaviour of the RE is missing.

Figure 14 shows the comparison between simulation and experiment as well as the modified Kelly model behaviour presented in Merzkirch et al.[15] for a reinforcing ratio of 11.1 vol.%. The modification of the analytical Kelly model is based on the introduction of the multiple necking of the RE in the plateau region. A very good agreement can be observed for the stress–strain curve calculated via simulation and the model for regions I and II. In comparison to the experimental curve a small overestimation of the stresses can be seen.

The simulation also shows a curved plateau region (region III), comparable to the experiment, although smaller stresses were calculated. Furthermore, the necking can be predicted precisely according to the stress reduction.

Table 3. Mechanical properties determined via experiment,[15] modified Kelly model[15] and simulation.

	E_I	E_{II}	$R_{p0.2}$	σ_{UTS}
	in GPa	in GPa	in MPa	in MPa
Experiment[15]	74	22	146	394
Mod. Kelly model[15]	82	24 (equation (2))	184	346 (equation (3))
Simulation	84	22	176	368

Table 3 lists the mechanical values from all the different methods. The values of the modified Kelly model were calculated using the rule of mixture and equation (2), deduced from the stress–strain response ($R_{p0.2}$). In particular, a good agreement can be observed for the stiffness E_I and E_{II}.

In contrast to the experiment, the predictions show an overestimation of the offset yield strength $R_{p0.2}$ and a conservative estimation of the composite tensile strength σ_{UTS}.

In the following, the calculated deformation and damage behaviour as a function of different total strains for a radial normal strength of $\sigma_{rad} = 2$ MPa will be explained in detail.

Figure 15 shows different quarter sections of the Mises stress as contour plots for different total strains. It can be concluded that already at a total strain of $\varepsilon_t = 4\%$ stresses of about 2000 MPa within the RE as well as stresses of 150 MPa within the matrix occur.

At a total strain of $\varepsilon_t = 9\%$, Figure 15(c), stress concentrations within the matrix and the RE can be seen. The resulting necking of the matrix' inner surface and the necking of the RE lead to a debonding of

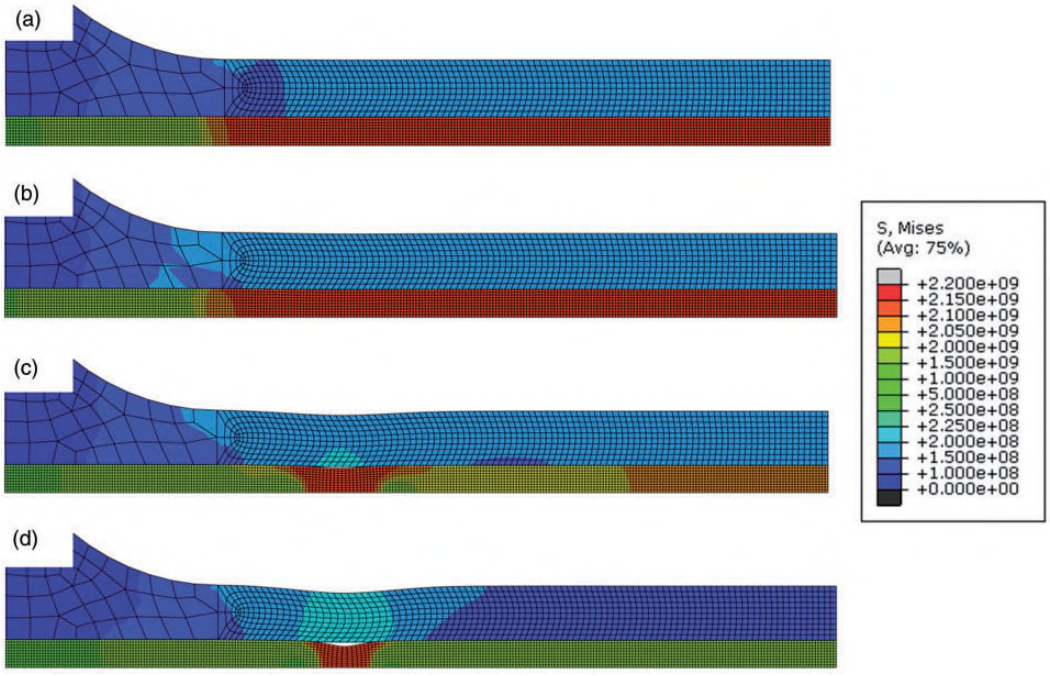

Figure 15. Calculated necking at different total strains ε_t of (a) 4%, (b) 7%, (c) 9%, (d) 10.3% (scale factor = 1) (Mises stress in Pa).

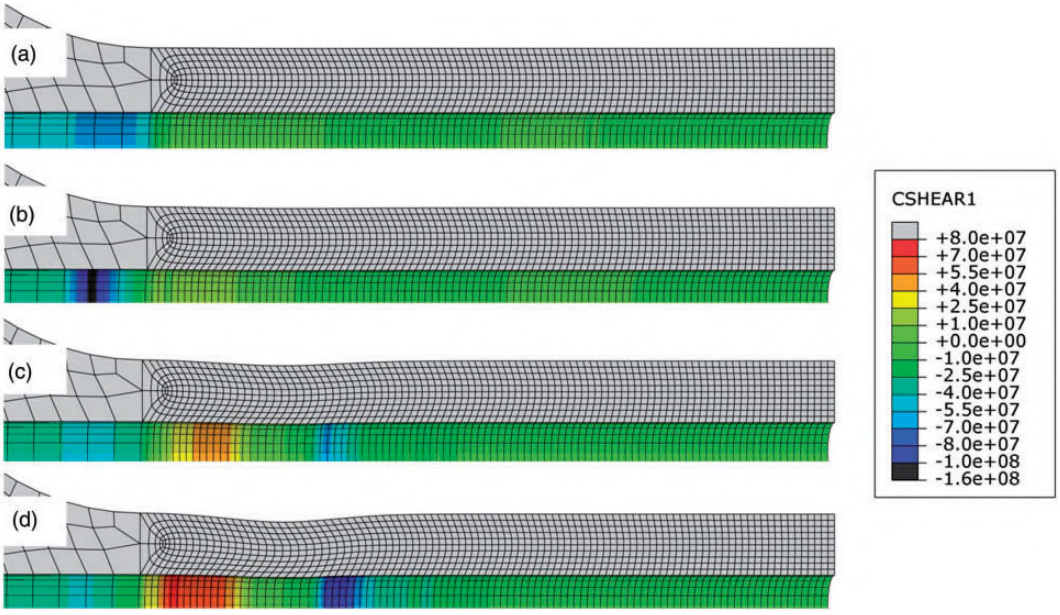

Figure 16. Calculated shear stress (in Pa) at different total strains ε_t of (a) 4%, (b) 7%, (c) 9%, (d) 10.3% (scale factor = 1).

the interface. Furthermore, small stresses occur in the homogenous deformed area of the measuring length of the RE and the matrix. Additionally, a necking of the matrix' outer surface can be seen. At a total strain of $\varepsilon_t = 10.3\%$ a more pronounced necking on both sides of the matrix can be seen. Due to the advanced necking of the RE an increase in the gap between matrix and RE can be observed. The load flow between matrix and RE, represented via the axial shear stress, is shown in Figure 16. At a total strain of $\varepsilon_t = 7\%$, Figure 16(b), within the transition area of the measuring length, high shear stresses can be found which decrease with increasing deformation. The remaining interface length shows almost homogenous shear stresses. Furthermore, it

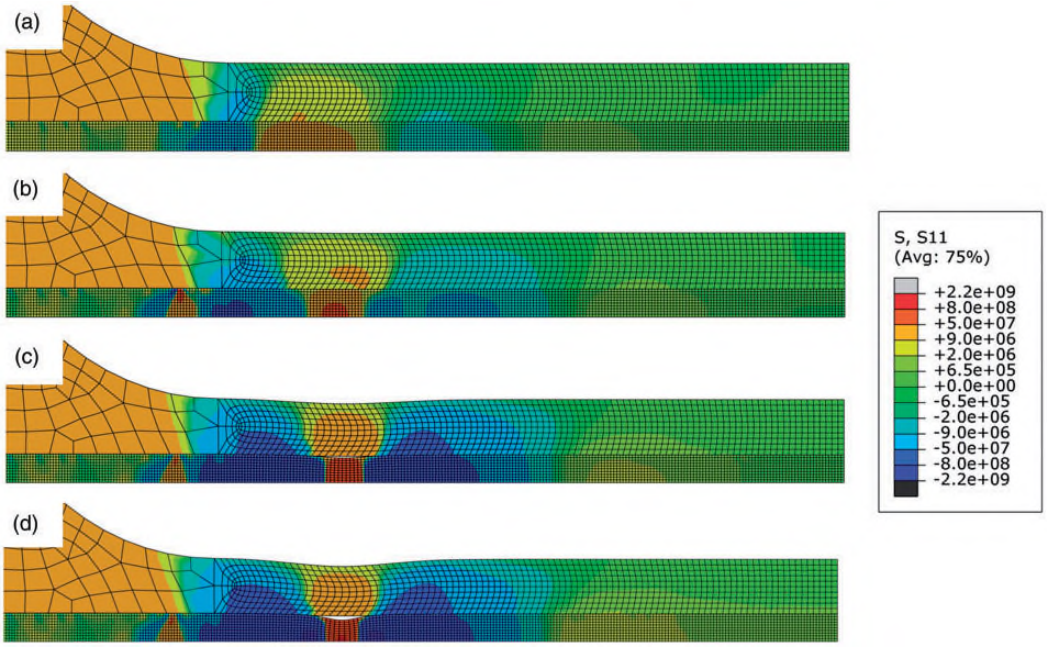

Figure 17. Calculated radial stress (in Pa) at different total strains ε_t of (a) 4%, (b) 7%, (c) 9%, (d) 10.3% (scale factor = 1).

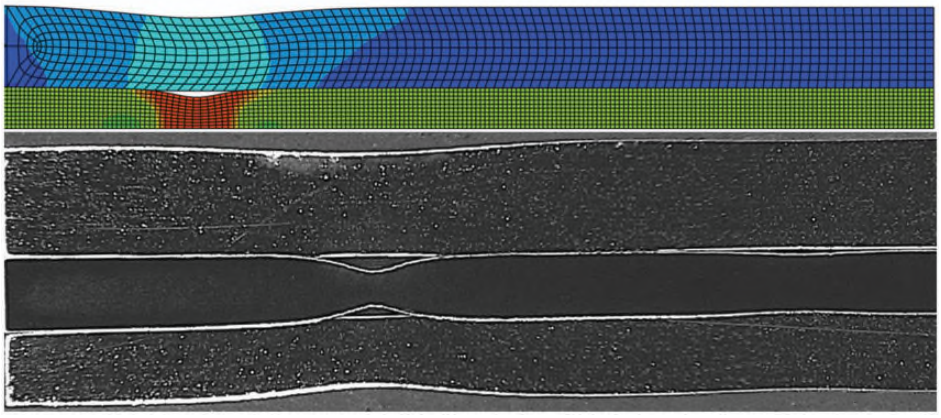

Figure 18. Comparison between calculated and experimentally determined damage (top: simulation $\varepsilon_t = 10.3\%$ scale factor = 1, below: longitudinal section $\varepsilon_t = 9\%$[15]).

should be noted that the larger element size in the clamping area in comparison to the adjacent measuring length does not have an influence on the results.

Starting from a strain $\varepsilon_t = 9\%$ high stress concentrations can be seen to the left and right of the necking area. The load flow continues within the specimen head from the matrix into the RE. It continues from the RE into the matrix right of the necking.

Figure 17 shows the radial stresses within the matrix and the RE for different total strains. At a total strain of $\varepsilon_t = 7\%$ high radial stresses close to the interface can be seen at the transition of the measuring length. Further stress concentrations can be observed in the necking region. Within the matrix and the RE tensile stresses can be observed, whereas the regions to the right and left of the RE necking area show high compressive stresses.

The calculated damage is compared to the longitudinal section (Figure 18). In contrast to the longitudinal section no multiple necking of the RE can be observed for the calculated damage. It should be mentioned that the comparison only shows a quarter section of the calculated area. Consequently, in a full section, two symmetric areas would be visible.

The most pronounced necking occurs closer to the specimen's transition area for the calculation in comparison to the experiment. Nevertheless, a good agreement between experiment and calculation of the two-sided necking of the matrix can be observed.

Further investigations have shown that the position of the necking is influenced by the clamping length of the specimen head and therefore by the load flow. It can also be observed that a smaller clamping length and clamping at a greater distance from the measuring length lead to a shift of the necking towards the specimen centre.

Conclusions

A good agreement between simulation and experiment for the tensile behaviour of 11.1 vol.% spring-steel (301SS)-wire-reinforced aluminium alloy EN AW-6082 can be shown. This was proved by means of quantitative values as well as qualitative deformation and damage behaviour until fracture of the RE (region III). The multiple necking of the reinforcing wire, which was confirmed experimentally, was also calculated in the simulation.

The modelling of the interfacial behaviour is based on many assumptions since more experimental data are needed – like the interfacial normal strength between matrix and reinforcement – which is limited and elaborate due to the small dimensions of the RE ($d = 1$ mm). This could be accomplished by a micromechanical determination of the radial properties of the interface, e.g. normal adhesion strength, in order to obtain detailed knowledge about the consistency and the mechanical behaviour of the interfacial region which is not currently available.

Further investigations should focus on the implementation of the residual stresses within the simulation and the analysis of the effect on the interfacial and deformation behaviour. The residual stress state – which results from forming, based on the high plastic deformation during the composite extrusion process, as well as from the coefficient of thermal expansion mismatch between the RE and the matrix material – has first been experimentally investigated in Weidenmann et al.[26]

Acknowledgment

This paper is based on investigations of the subproject A3 – 'Material systems for reinforced and functional extruded profiles' – of the Collaborative Research Center/Transregio 10 which is kindly supported by the German Research Foundation (DFG).

Conflict of interest

None declared.

References

1. Kleiner M, Schomäcker M, Schikorra M, et al. Manufacture of extruded and continuously reinforced aluminium profiles for ultra-lightweight constructions. *Materialwiss Werkst* 2004; 35: 431–439.
2. Weidenmann KA, Schomäcker M, Kerscher E, et al. Composite extrusion of aluminium matrix specimens reinforced with continuous ceramic fibres. *Light Metal Age* 2005; 63: 6–10.
3. Merzkirch M, Weidenmann KA, Kerscher E, et al. Mechanical properties of hybrid composite extrusions of an aluminium-alumina wire reinforced aluminium alloy. In: *Materials Science and Technology (MS&T)*. Pittsburgh, 2008, pp.2552–2562.
4. Schomäcker M, Schikorra M and Kleiner M. 4 years of research on composite extrusion for continuous reinforcement of aluminium profiles. In: *6th Aluminium Two Thousand World Congress*. Florence (Italy), 2007.
5. Pietzka D, Schikorra M and Tekkaya AE. Embedding of alumina reinforcing elements in the composite extrusion process. *Adv Mater Res* 2008; 43: 9–16.
6. Pietzka D, Khalifa NB, Gerke S, et al. Composite extrusion of thin aluminium profiles with high reinforcing volume. *Key Eng Mater* 2013; 554–557: 801–808.
7. Marshall DB. An indentation method for measuring matrix-fibre frictional stresses in ceramic composites. *Commun Am Ceram Soc* 1984; C-259–C-260.
8. Marshall DB and Oliver WC. Measurement of interfacial mechanical properties in fiber-reinforced ceramic composites. *J Am Ceram Soc* 1987; 70: 542–548.
9. Weidenmann KA, Kerscher E, Schulze V, et al. Characterization of the interfacial properties of compound-extruded lightweight profiles using the push-out-technique. *Mater Sci Eng* 2006; A 424: 205–211.
10. Janczak J, Rohr L, Schulz P, et al. Grenzflächenuntersuchungen an endlosverstärkten aluminium-Verbundwerkstoffen für die Raumfahrttechnik. *Oberflächen Werkstoffe* 1995; 6: 16–19.
11. Pochirajua KV, Tandonb GP and Pagano NJ. Analyses of single fiber pushout considering interfacial friction and adhesion. *J Mech Phys Solids* 2001; 49: 2307–2338.
12. Tandona GP and Pagano NJ. Micromechnical analysis of the fiber push-out and re-push-out test. *Compos Sci Technol* 1998; 58: 1709–1725.
13. Yue CY, Lee LL and Sano T. Experimental push out testing and analysis of fibre reinforced composites: Applicability and test considerations. *Mater Sci Technol* 1998; 14: 987–1000.
14. Theler JJ, Wagner A and Ames A. Herstellung von aluminium/Stahl-Verbundstromschienen mit metallurgischer Bindung zwischen Aluminium und Stahl durch Verbundstrangpressen. *Metallwiss Technik* 1976; 3: 223–227.
15. Merzkirch M, Meissner M, Schulze V, et al. Tensile behaviour of spring steel wire reinforced EN AW-6082. *J Compos Mater* 2015; 49: 261–274.
16. Kelly A and Davies J. The principles of the fibre reinforcement of metal. *Metall Rev* 1965; 10: 1–78.

17. Courtney TH. *Mechanical behavior of materials*. Boston: McGraw Hill, 2nd ed., 2000.
18. Chandra N and Ananth CR. Analysis of interfacial behavior in MMCs and IMCs by use of thin-slice push-out tests. *Compos Sci Technol* 1995; 87–100.
19. Abaqus 6.9.1 Documentation, 2009.
20. Chandra N. Evaluation of interfacial fracture toughness using cohesive zone model. *Composites: Part A* 2002; 33: 1433–1447.
21. Mukherjee S, Ananth CR and Chandra N. Evaluation of fracture toughness of MMC interfaces using thin-slice push-out tests. *Scr Mater* 1997; Bd. 11: 1333–1338.
22. Yuani M, Yang Y, Huang B, et al. Evaluation of interface fracture toughness in SiC fiber reinforced titanium matrix composite. *Trans Nonferrous Met Soc China* 2008; 18: 925–929.
23. Yuan MN, Yang YQ and Luo HJ. Evaluation of interfacial properties in SiC fiber reinforced titanium matrix composites using an improved finite element model. *Mater Character* 2008; 59: 1684–1689.
24. Wisnom MR. Modelling fibre-matrix interface failure in unidirectional metal matrix composites. In: *Presented at 2nd International ABAQUS Users Conference*. Stresa, 1989.
25. Li DS and Wisnom MR. Factors controlling the transverse tensile properties of unidirectional SiC/Ti-6Al-4V. *Compos Eng* 1995; 5: 235–255.
26. Weidenmann KA, Fleck C, Schulze V, et al. Analysis of the microstructure and the residual stress state of aluminium extrusions reinforced with rope. *Materialwissenschaft und Werkstofftechnik* 2005; 36(7): 307–312.